ISSN 1063-7737, Astronomy Letters, 2017, Vol. 43, No. 11, pp. 768–779. © Pleiades Publishing, Inc., 2017.
Original Russian Text © N.M. Firstova, V.I. Polyakov, 2017, published in Pis'ma v Astronomicheskii Zhurnal, 2017, Vol. 43, No. 11, pp. 845–856.

Structure and Physical Conditions in the Hα Loops of an M7.7 Solar Flare

N. M. Firstova* **and V. I. Polyakov****

Institute of Solar–Terrestrial Physics, Russian Academy of Sciences, Siberian Branch, P.O. Box 4026, Irkutsk, 664033 Russia

Received March 23, 2017

Abstract—The M7.7 solar flare on July 19, 2012, is the most dramatic example of a "Masuda" flare with a well-defined second X-ray above-the-loop-top source. The behavior of the system of loops accompanying this flare has been studied comprehensively by Liu et al. based on Reuven Ramaty High Energy Solar Spectroscopic Imager (RHESSI) and Solar Dynamics Observatory/Atmospheric Imaging Assembly (SDO/AIA) data. We have performed spectroscopic and filter observations of the Hα loops in this flare with the Large Solar Vacuum Telescope. The basic physical parameters in the loops of this peculiar flare generally coincide with the known data in Hα loops. However, the electron density, 10^{11} cm^{-3}, and the integrated disk-center continuum intensity, 12%, are quite high, given that the observations were obtained almost 3 h after the flare onset. We have estimated the ascending velocity of the loop arcade ($\sim$3.5 km s^{-1}) and the height difference between the Hα and 94 Å loops ($\sim 2 \times 10^4$ km).

DOI: 10.1134/S1063773717110032

Keywords: *flare loops, spectral line, electron density.*

1. INTRODUCTION

We observed the system of post-flare loops accompanying the July 19, 2012 flare on the southwestern limb with the Large Solar Vacuum Telescope (LSVT) in the spectrum and using a birefringent filter in Hα. Hot ($T > 10^5$ K) coronal loops have been studied extensively both theoretically and observationally, and there are several extensive reviews on this subject (see, e.g., Reale 2014). In particular, this review presents the classification of loops by temperature: hot, warm, and cool, from 2 to 0.1 MK. Loops with temperatures 2×10^4 K $< T < 10^5$ K, which are also studied using EUV and UV lines, belong to the cool loops. Heinzel (1994) proposed to call even cooler loops with $T < 2 \times 10^4$ K, which are visible in Hα, Hα loops. A special class of post-flare loops observed during and after a flare, also called Hα loops (or cool flare loops), was described by Svestka et al. (1987, 1989), Heinzel et al. (1992), and Schmieder et al. (1995). Simultaneous Hα observations as well as ultraviolet and X-ray observations have long shown that the flare loops are an extension, i.e., actually a natural part of the solar flare proper (Svestka et al. 1987; Heinzel 1994).

All of the plasma parameters (temperature, pressure, density) that determine the physical structure of cool loops were quantitatively estimated in the above few papers. A gas pressure $P_g \sim 3$ dyn cm^{-2} and, accordingly, an electron density $n_e \sim 10^{12}$ cm^{-3} at a temperature $T \sim (1–1.5) \times 10^4$ K were obtained for disk Hα loops (Svestka et al. 1987; Heinzel and Karlicky 1987). Such a gas pressure is needed for the disk loops to be visible in emission. $P_g \sim 0.1–0.5$ dyn cm^{-2} and $n_e \sim 10^{11}$ cm^{-3} are sufficient for the loops on the disk to be visible in absorption (Heinzel et al. 1992). Using spectroscopic observations and NLTE (in the absence of local thermodynamic equilibrium) plasma simulations in prominences, Schmieder et al. (1995) made a relative estimate of the electron density (2.2×10^{10} cm^{-3}) in a limb flare. When combining Hα observations with SXT images, Schmieder et al. (1995) obtained a relationship between the cold and hot plasmas. The electron density in the hot loops of the same flare is 7×10^9 cm^{-3}, while the temperature of the hot X-ray loops is $\sim 5.5 \times 10^6$ K.

In principle, the probability of observing the flare Hα loops is higher than the probability of observing the flares proper, because the loops are long-lived features and may persist for >10 h (Schmieder et al. 1995). However, in recent years there have

*E-mail: first@iszf.irk.ru
**E-mail: polyak@iszf.irk.ru

been few optical observations and they mainly concern other objects of solar activity: flares and prominences (Milic et al. 2009). The most detailed study in optical lines, including Hα, was carried out by Li et al. (2005) for the limb flare on August 1, 2003. The loops in white light and Hα were compared by You et al. (2003). Kotrc et al. (2013) modeled the Hα-eruptive events observed on the solar limb. By comparing the Hα (without any line profiles) and soft X-ray images, Kamio et al. (2003) determined the cooling time of the post-flare loops.

The Hα loops we observed accompanied a Masuda-type flare. Several observations of such flares that show bright hard X-ray (HXR) sources above the main loop top are known (see, e.g., Masuda et al. 1994; Tomchak 2001, 2009; Petrosian et al. 2002; Ishikawa et al. 2011; Chen and Petrosian 2012). The M7.7 flare under consideration is unique in that it is the best example of such flares, where the second upper X-ray source, the so-called above-the-loop-top source, has been detected most clearly. This possibly explains the presence of high Hα loops 3 h after the flare onset. It is probable that we observed the loops even not on the limb but behind the limb, but they could be seen, because the so dense and cool loops were located quite high.

Furthermore, this secondary source was simultaneously observed by the Reuven Ramaty High Energy Solar Spectroscopic Imager (RHESSI) and the Solar Dynamics Observatory/Atmospheric Imaging Assembly (SDO/AIA). The events in the corona lasted for a fairly long time: at least the ultraviolet loops ceased to be visible at ∼10 UT, while their maximum emission was at ∼6 UT. According to Solar Terrestrial Relations Observatory (STEREO) observations, the Hα loops were clearly seen until 09:45 UT, and one faint loop was seen until 11:26 UT.

Such a unique flare could not but interest scientists. Using RHESSI and SDO/AIA observations, Krucker and Battaglia (2014) made the first direct measurements of the density of thermal protons and the density of nonthermal electrons in the above-the-loop-top source. The post-flare hot coronal loops in this flare were described by Liu et al. (2013). In particular, the authors determined the primary loci of particle acceleration and plasma heating with respect to the magnetic reconnection site. Gritsyk and Somov (2016) applied an analytical model of the kinetic behavior of accelerated electrons for this flare. Using the thick-target approximation with a reverse current for the chromospheric HXR source and the thin-target approximation for the coronal one, they obtained estimates of the slopes of the HXR spectra for both sources consistent with observations.

In our paper we are going to expand the data on the loops accompanying the M7.7 flare on July 19, 2012, to include the data on the cooler part of these loops using both spectroscopic and filter observations. The fairly high spatial and spectral resolutions of the LSVT (Skomorovsky and Firstova 1996) allow a spatial comparison of the simultaneously observed hot and cool loops to be made. Our filter and spectroscopic observations of the Hα loops with the LSVT are described in Section 2. The results of our primary reduction of these observations are given in Section 3. The parameters of the Hα profiles are determined in Section 4, and the physical conditions of the plasma in the loops are estimated on this basis in Section 5. A discussion of the results and our conclusions are presented in Section 6.

2. OBSERVATIONS

2.1. Description of the Filter Observations

The Hα loops observed with the LSVT after the M7.7 flare occurred at ∼04:17 UT on July 19, 2012, (the appearance of X-ray and ultraviolet emission at the loop top) in the active region (AR) NOAA 11520 on the southwestern limb were the subject of our study. The loops proper lit up later, with the onset time of maximum intensity having increased from ∼05:50 UT for the 193 Å line to ∼06:40 UT for the 171 Å line. Apart from imaging the loop at the Hα center in the light reflected from the spectrograph mirror slit with a Princeton Instruments (512 × 512) CCD camera, we carried out spectroscopic observations in Hα using a wide-field Fligrab CCD camera (2048 × 2048, 40 mm in diameter). The time interval of these observations 06:54:26–07:28:18 UT is within the time (from ∼04 to ∼10 UT) of the investigation of hot loops (Liu et al. 2013).

Since the Princeton Instruments frame cuts out 69.42″ solar images on the spectrograph slit, the loop image taken with the Princeton Instruments CCD did not completely fit into the frame, and the image of the Hα loops in Fig. 1 is composed of two frames. The position of the spectrograph slit is seen in Fig. 1, and the loop median is drawn by the black line to approximately determine the loop height. The loop height determined from this figure (for 06:55:56 UT) is ∼56.8″ or ∼42 000 km. At this time, the loops in the ultraviolet lines were considerably higher, while ∼1 h later their height in the 94 Å line was ∼90″ (see Fig. 9). This is consistent with other observations. Svestka et al. (1987) described the observations of a rich system of Hα loops whose tops rose from a height of 25 000 to 55 000 km in 90 min. At the same time, Schmieder et al. (1995) pointed out that a few minutes after the occurrence of two-ribbon flares dense cool plasma loops appear connecting the two ribbons. The height of such loops can reach an altitude of

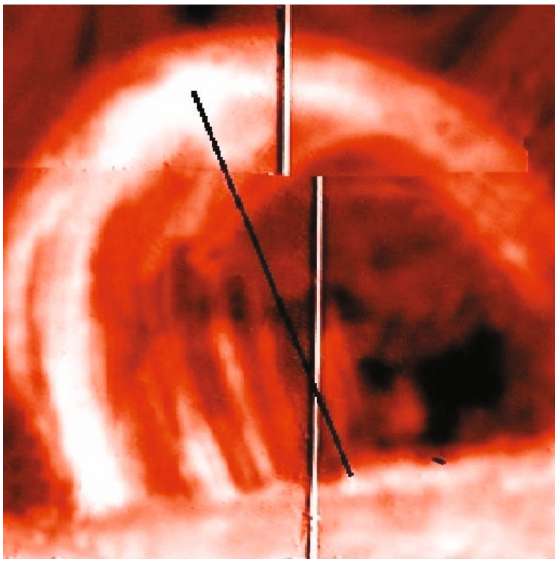

Fig. 1. (Color online) Image of the loops at 06:55:56 UT at the Hα center. The vertical straight lines are the images of the spectrograph slit. The inclined black straight line is the median of the first visible loop.

100 000 km and the distance between the ribbons increases with time after the flare maximum, first rapidly ($\sim$50 km s^{-1}), then more slowly ($\sim$1 km s^{-1}). The loop diameter is approximately the same in the legs and at the top: it is 8500 km in the legs, 3800 km in the brightest part, and 11 400 km at the top.

Apart from the main, northern leg, other, remote northern legs are also visible, while the southern legs appear to have already gone behind the western limb.

It should be noted that our images of the loops did not reveal any dynamic changes in their behavior for half an hour.

2.2. Description of the Spectroscopic Observations

The method of spectroscopic observations should be described in more detail. It can be seen from Fig. 1 that a minor part of the loop falls into the spectrograph slit. During the observations we attempted to place different parts of the loop in the slit by moving the loop image and recording this position on the Princeton Instruments camera. Consequently, the time interval between the frames with the loop image was not constant. The spectrum was taken on the Fligrab CCD automatically 12 s later. Thus, we obtained much more spectra than loop images.

Four spectra were simultaneously taken on the screen of the Fligrab camera; as a consequence, the actual height of the slit transmitting the light into the spectrograph was smaller than that in Fig. 1, being $\sim$1/4 of the image height on the Princeton Instruments frame. This is because the spectrograph was set for spectropolarimetric observations of solar flares. The observations were carried out in two spectral lines (Hα and Fe I 6302 Å) using two camera mirrors. Beam-splitting polarization optics was set behind the spectrograph slit. The technique of spectropolarimetric observations at the LSVT is described in Firstova et al. (2008, 2014). During our observations we detected no polarization in any of these two lines. Moreover, when the slit was crossing the loops lying in the corona, the Fe I 6302 Å line was not visible at all.

Figure 2 presents images of the spectrograms in the loops. Above we pointed out that the height of the spectrum is only 1/4 of the height of the spectrograph mirror slit shown in Fig. 1. Therefore, Fig. 2a shows the spectrum taken in the upper part of Fig. 1 and only the loop top falls into the spectrograph. Figure 2b shows the spectrum taken in the lower part of Fig. 1 and part of the photosphere and the lower part of the loop fall into the spectrograph.

3. RESULTS OF THE PRIMARY REDUCTION

The Hα profiles in the loops were obtained from the cuts made across the spectrograph slit. It can be shown that each measured area on the Sun was $\sim 0.34'' \times 0.34''$: the slit width was 0.07 mm (1 mm on the spectrograph slit is $\sim 4.8''$) and the cut height on the spectrogram was 5 pixels (1 pixel is $0.0686''$). From 3 to 6 cuts were drawn on each spectrogram; the separation between them was chosen arbitrarily. Apart from the cuts across the loops, we made cuts in the quiet photosphere on the disk and in the chromosphere at the disk edge. Figures 3a–3d present examples of the Hα profiles in the photosphere, the chromosphere, and the loops.

In Fig. 3 the center of the unshifted Hα line found from the reference lines is marked by zero. It can be concluded from Fig. 3 that the Hα profiles in the photosphere and the chromosphere virtually coincide with the center of the unshifted line or are slightly redshifted. The more intense line profiles in the loops are shifted insignificantly, while the weaker line profiles in the loops have a significant blueshift.

Unfortunately, only a small fraction of the spectrograms coincided in time with the filtergrams. Therefore, we attempted to determine some of the parameters from all Hα profiles by separating them only by objects: in the loop, the photosphere, and the chromosphere. Figure 4 shows a correlation between velocities V (km s^{-1}) and equivalent widths W (Å) for all cuts. The cuts in the photosphere are represented by the diamonds. The mean velocity in the photosphere is 1.54 ± 0.289 km s^{-1}, corresponding to

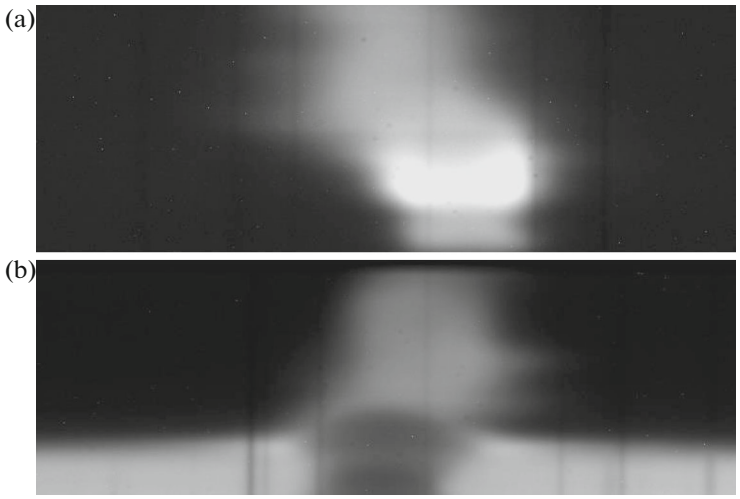

Fig. 2. Images of the spectrograms near Hα: (a) the spectrum at the loop top, (b) the spectrum in the photosphere and the loop leg.

the rotation velocity of the Sun on the western limb (a positive velocity).

The scatter of velocities in the loops is large, but it decreases noticeably with increasing equivalent width. Most of the velocities are negative.

Our filter images of the loops in Hα show that the loops are spatially inhomogeneous. It can also be seen from Figs. 3c and 3d that the line profiles obtained from one spectrogram differ significantly. We divided all Hα profiles in the loops into three groups. The profiles mostly had a shape corresponding to Doppler broadening. We divided them into two groups: A with a relative intensity <1.5 and B with a relative intensity ≥ 1.5. Group C included the profiles with characteristic features (the profiles with a red or blue asymmetry and the profiles with a significant self-reversal).

It has been pointed out above that we were able to "tie" only some of the spectrograms to the loop image on the spectrograph slit. Furthermore, a comparison of the frames themselves with one another also caused difficulties: first it was necessary to display the slit positions for all frames in one figure and then to indicate the positions of the cuts over the slit by the dots. Figure 5 shows the positions of all those Hα profiles for which we were able to determine the location in the image of the loops on the filtergrams. Here, the X coordinate corresponds to the position of the spectrograph slit on the filtergram, while the Y coordinate corresponds to the position of the cut on the slit along the dispersion. In addition, the diamonds, triangles, and circles in Fig. 5 mark the locations of the Hα profiles belonging to groups A, B, and C, respectively.

It can be seen from Fig. 5 that there are no profiles of group A at the loop footpoints, while there are all groups of profiles at the loop top.

Table 1 presents the mean parameters of all the measured profiles, including those for which the position was not determined. The number of profiles in each group is shown; the mean values of the relative intensity, the equivalent width, the full width at half maximum (FWHM) of the line profile, and the line-of-sight velocities are given. The root-mean-square deviations were calculated for all values.

The parameters of the profiles in the loops derived from our observations are consistent with the previous results of Hα loop studies: the relative intensity varies from 0.6 (loops on the disk in absorption) to 2 and the FWHM is observed in the range 1–1.5 (Svestka et al. 1987; Heinzel et al. 1992; Schmieder et al. 1995). The line-of-sight velocities in all three groups of profiles are, on average, negative. During our observations, according to the STEREO data, the Hα loops were before the limb; therefore, negative velocities suggest an upflow in the loops. Meanwhile, Heinzel et al. (1992) and Schmieder et al. (1995) showed the vertical downflow velocity to be 70–80 km s^{-1}, with it being higher in the legs than at the top.

4. DETERMINING THE PARAMETERS $\Delta\lambda_D$, τ_0, $\bar{S}$, AND v_c IN THE Hα PROFILES IN LOOPS

To interpret the line profiles in a loop, we can use the intensity expression for a limb flare, i.e., disregard the background intensity (Smith and Smith 1966):

$$I_\lambda = \bar{S}(1 - e^{-\tau_\lambda}), \quad (1)$$

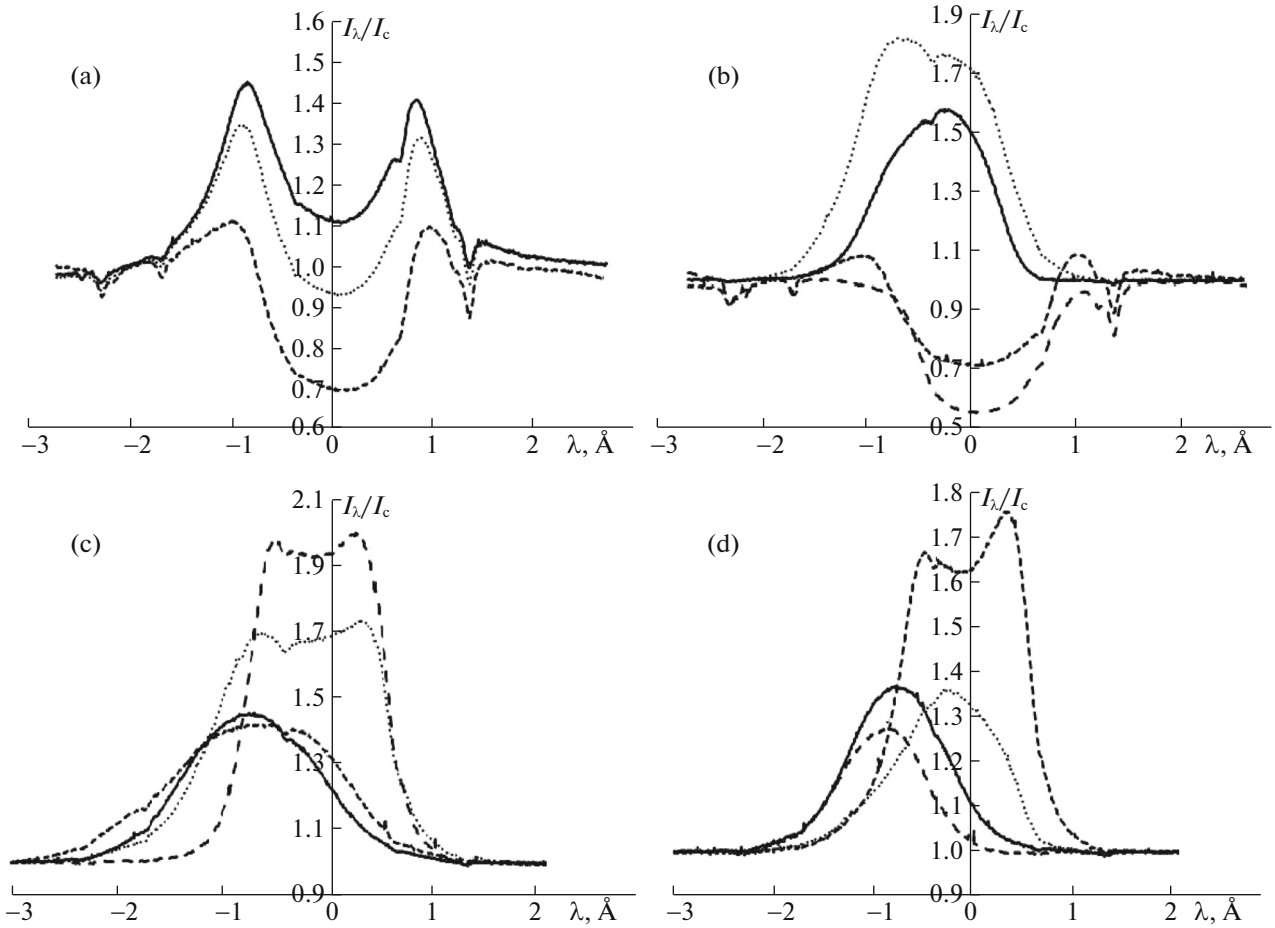

Fig. 3. Profiles: (a) Hα in the quiet photosphere and the chromosphere; (b) Hα in the quiet photosphere and the loops; (c, d) Hα in several cuts across the loops.

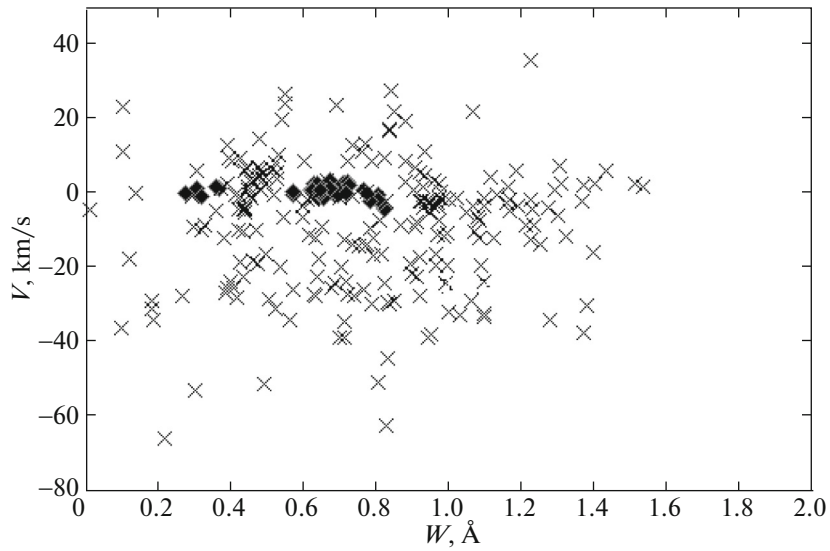

Fig. 4. V versus W (Å). The diamonds and crosses refer to the cuts in the photosphere and the loops, respectively.

Table 1. Observed characteristics of the three groups of Hα profiles in the loops

Parameter	A (95 profiles)	B (75 profiles)	C (67 profiles)
I_λ/I_c (mean)	1.37 ± 0.011	1.59 ± 0.008	1.71 ± 0.015
W, Å	0.48 ± 0.020	0.84 ± 0.022	1.10 ± 0.024
FWHM, Å	1.18 ± 0.038	1.46 ± 0.074	1.56 ± 0.030
V (LOS), km s^{-1}	-16.36 ± 1.900	-0.96 ± 1.790	-2.14 ± 1.013

where τ_λ is the total optical depth in the flare along the line of sight and $\bar{S}$ is the average source function. Strictly speaking, any interpretation of the line profiles is associated with some assumptions. This also concerns the source function that is not constant with depth, especially for lines with a self-reversal.

The profiles observed in a loop were bell-shaped, suggesting a Gaussian (Doppler) broadening. This corresponds to a linear relation between $\log\tau_\lambda$ (or $\log(I_\lambda - I_c)$ or $\log(I_\lambda/I_c - 1)$) and λ^2. Taking the logarithm of the formula for the optical depth, as, for example, in P. Mein and N. Mein (1988) and Kotrc et al. (1994):

$$\tau_\lambda = \tau_0 e^{-(\Delta\lambda/\Delta\lambda_D)_2}, \qquad (2)$$

we can obtain the Doppler half-width $\Delta\lambda_D$ from any of the following formulas:

$$\Delta\lambda_D = \sqrt{\frac{\Delta\lambda^2}{-\ln(I_\lambda - I_c)}} \qquad (3)$$

or

$$\Delta\lambda_D = \sqrt{\frac{\Delta\lambda^2}{-\log(I_\lambda - I_c)}\log e}.$$

Figure 6 shows an example of determining $\Delta\lambda_D$ from observations, where $\Delta\lambda_D$ was determined from the linear segment of the line.

Knowing $\Delta\lambda_D$ allows τ_λ to be estimated from Eq. (2) for a specified τ_0, where τ_0 is the optical depth at the line center. By varying $\bar{S}$ and τ_0, the observed profile can be reconstructed using Eq. (1).

To determine $\Delta\lambda_D$, $\bar{S}$, and τ_0, we chose two profiles for each of groups A–C. Based on each of the chosen profiles, we plotted graphs similar to those

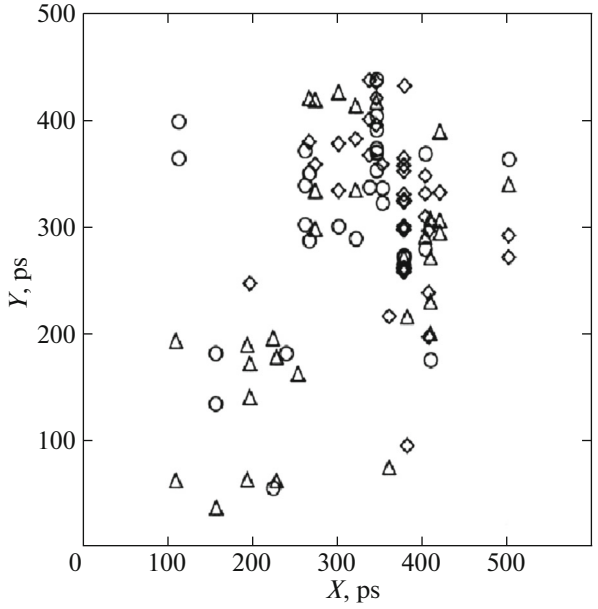

Fig. 5. Location of the derived Hα profiles of groups A, B, and C from the combined filtergram (the diamonds, triangles, and circles, respectively).

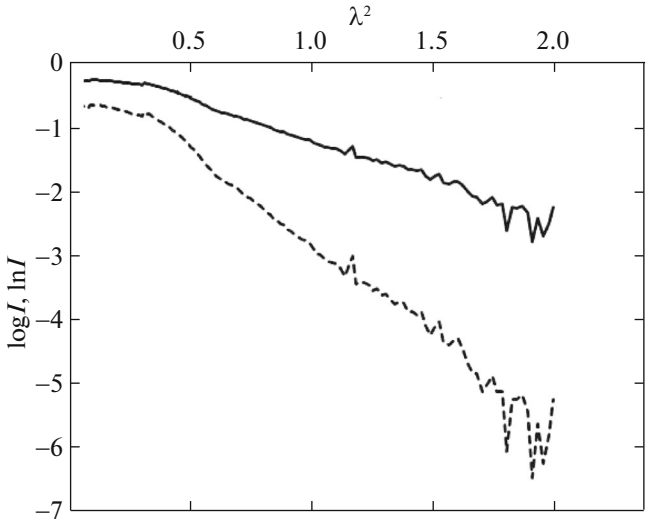

Fig. 6. Dependence of $\log(I_\lambda - I_c)$ and $\ln(I_\lambda - I_c)$ on $\Delta\lambda^2$. The solid and dashed lines correspond to $\log(I_\lambda - I_c)$ and $\ln(I_\lambda - I_c)$, respectively.

Table 2. Calculated parameters of the Hα profiles in a loop for the three groups of profiles

Parameter	A (95 profiles)		B (75 profiles)		C (67 profiles)	
$I_\lambda/I_c - 1$	0.467	0.334	0.519	0.59	0.684	0.856
$\Delta\lambda_D$, Å	0.672	0.536	0.647	0.578	0.835	0.73
$\bar{S}$	0.5	0.42	0.62	0.675	0.71	0.88
τ_0	2.5	2	2.0	2.0	5.0	9.0
v_c					13.8 km s^{-1}	16.6 km s^{-1}

presented in Fig. 6 to determine $\Delta\lambda_D$ from observations. Then, for the known $\Delta\lambda_D$ we selected $\bar{S}$ and τ_0 so that the line profile constructed with these data coincided with the chosen observed profile. Figures 7a–7f present examples of such a profile reconstruction.

It turned out that not all of the profiles could be reconstructed in this way. All profiles of group C appear bell-shaped almost without any wings. In this case, the Doppler half-width $\Delta\lambda_D$ derived from Eq. (3) and a graph similar to Fig. 6 cannot reconstruct the observed profile. To obtain the necessary steepness of the profile, the current value of $\Delta\lambda = \lambda - \lambda_0$ should be replaced by $\Delta\lambda = \lambda - \lambda_0 - \frac{v_c}{c}\lambda$ (P. Mein and N. Mein 1988; Heinzel et al. 1992). Here, v_c is the velocity of the line-forming material, c is the velocity of light, and λ is the wavelength of the line (in our case, Hα) center. This additional velocity is assumed to stem from the fact that the atoms moving along the line of sight exert a greater influence on the formation of the line profile than do the remaining atoms. This velocity is also called the "characteristic" one. According to H. Smith and E. Smith (1966), it can reach ~100 km s^{-1} in flares. The next two figures for the profiles of group C demonstrate the reconstructed profiles corrected for this additional velocity.

The parameters of the reconstructed Hα profiles in the loops are given in Table 2. For each of the groups the calculations were performed only for two profiles whose reconstruction is shown in Figs. 7a–7f.

For comparison, note that the Doppler width of the Hα profiles measured in cool flare loops on the disk varies from 0.5 to 2 Å, while the so-called characteristic velocity lies within the range 9–42 km s^{-1} (Heinzel et al. 1992).

5. ESTIMATING THE PHYSICAL CONDITIONS OF THE PLASMA IN Hα LOOPS

5.1. Estimating the Kinetic Temperature and Microturbulent Velocity

Knowing the Doppler half-width allows the temperature and microturbulent velocity (or the thermal and nonthermal velocities) to be estimated from the Hα profiles using the formula

$$\frac{\Delta\lambda_D}{\lambda_0} = \left(\frac{1}{c}\right)\sqrt{\xi^2 + 2\frac{kT}{m}}. \qquad (4)$$

This estimate is usually made as follows: Eq. (4) is rewritten as two Eqs. (5); the upper temperature limit is assumed and the microturbulent velocity is neglected in the first equation and vice versa in the second one:

$$\frac{\Delta\lambda_D}{\lambda_0} = 7\times10^{-7}\sqrt{T} \quad \text{and} \quad \frac{\Delta\lambda_D}{\lambda_0} = \frac{\xi}{c}. \qquad (5)$$

The first row in Table 3 gives the mean $\Delta\lambda_D$ for groups A, B, and C taken from Table 2. The next rows present the limiting maximum temperatures and microturbulent velocities calculated from $\Delta\lambda_D$. Since the temperature $T = 2\times10^4$ K is maximal for Hα loops, we considered the cases with a lower mean temperature common to all groups and equal to 1.5×10^4 and 1.0×10^4 K. It seems reasonable to take a temperature of 1.5×10^4 K. The microturbulent velocity will then exceed 20 km s^{-1} only in the loops of group C. This case is apparently more likely, because the microturbulent velocities turn out to be too high at a mean temperature of 10^4 K. For group C we took $T = 1.6\times10^4$ K; the microturbulent velocity will then be <20 km s^{-1}. T and ξ for this case are presented for different groups in the same rows in parentheses as the maximum ones.

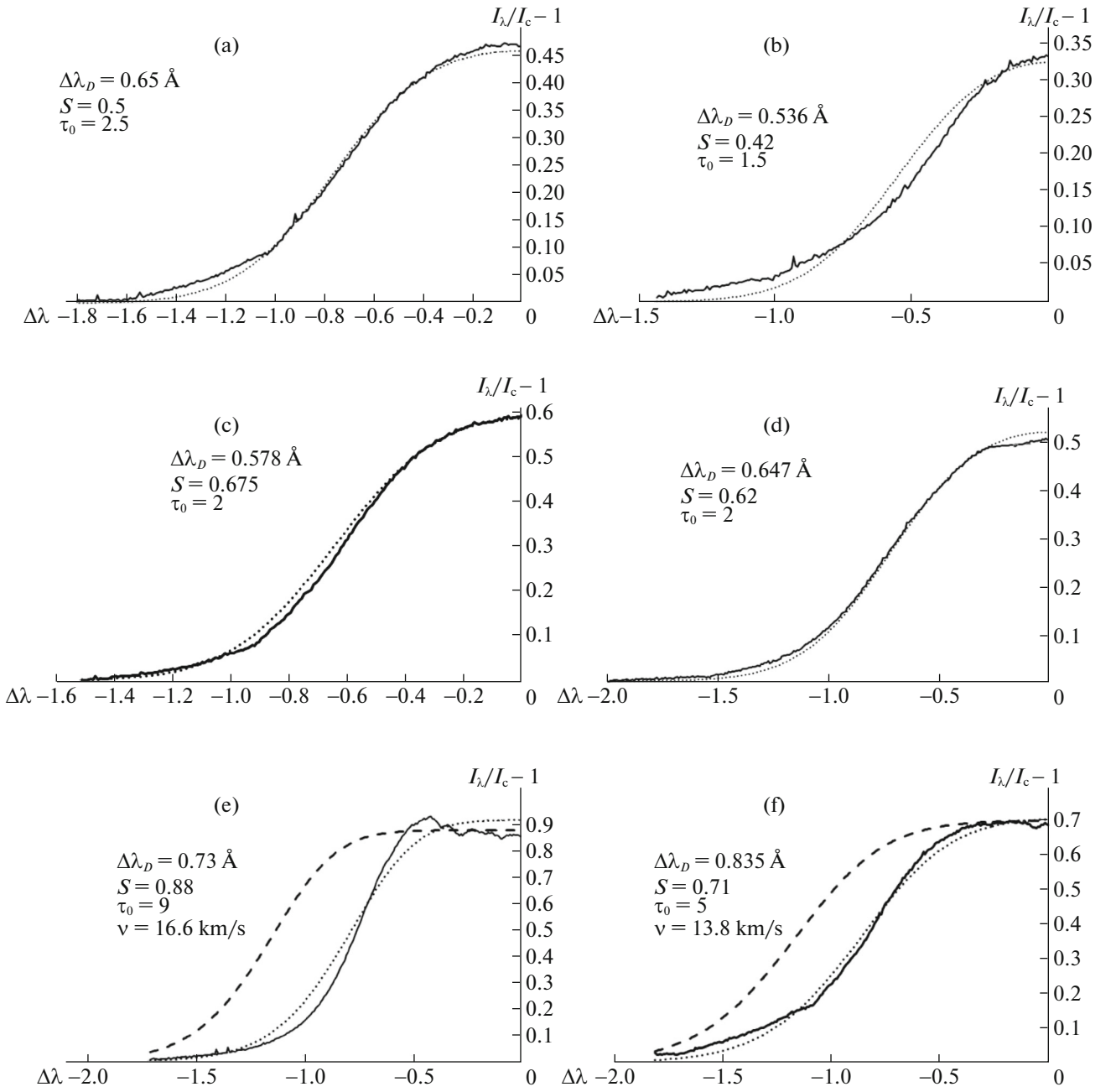

Fig. 7. Reconstructed profiles: (a, b) group A; (c, d) group B; (e, f) group C. The solid and dotted lines correspond to the observed and reconstructed profiles, respectively; the dashed line indicates the reconstructed profile without $\Delta\lambda = \frac{v_c}{c}\lambda$.

Indeed, as was noted in previous studies (Svestka et al. 1987; Heinzel and Karlicky 1987; Heinzel et al. 1992; Schmieder et al. 1995), although the temperature in Hα loops can vary within the range (8×10^3–2×10^4 K), the most realistic temperature lies within the range $(1–1.5) \times 10^4$ K. In this case, the microturbulent velocity is assumed to be <20 km s^{-1} (Svestka et al. 1987; Schmieder et al. 1995).

5.2. Determining the Geometrical Depth of a Loop z

Given the optical depth of the formation of the entire profile and writing a formula for it in the form

$$\tau_0 = \int_0^{\max} n\sigma dx, \qquad (6)$$

we can express the geometrical depth as $z = x_{\max} - x_0$. We assume that n (density) and σ (absorption co-

Table 3. Estimates of physical parameters for the plasma in loops from the reconstructed Hα profiles

Parameter	A (95 profiles)	B (75 profiles)	C (67 profiles)
$\Delta\lambda_D$	0.59	0.61	0.78
T, K	2.13×10^4 (1.5×10^4)	1.78×10^4 (1.5×10^4)	2.89×10^4 (1.5×10^4)
ξ, km s^{-1}	30 (16.8)	28 (11.1)	35.7 (24.8)
Z, km	90	125	590
E, cgs	1.54×10^5	2.69×10^5	3.52×10^5
$E/I_{\mathrm{c}.C}$, %	5.4	9.5	12.4
$\log EM$	29.1	29.7	30
EM, cm^{-3}	$10^{29.1}$	$10^{29.7}$	10^{30}
D, km	180–270	250–375	1180–1770
n_e, cm^{-3}	$(8.36–6.83)\times10^{10}$	$(1.42–1.16)\times10^{11}$	$(9.2–7.5)\times10^{10}$

efficient) are constant over the entire formation depth of the line profile. Suppose that for the geometrical depth $x_0 = 1$ km the optical depth can be written as

$$\tau_1 = \int_0^{x_0} n\sigma dx. \qquad (7)$$

Dividing τ_0 by τ_1, we will then obtain $x_{\max} \sim z$ (km). For all of the constructed profiles we assumed that the relative intensity of the line (or $\bar{S}$), 0.01 (i.e., almost invisible), is at a depth x_0. The geometrical depth of the loops obtained in this way from Figs. 7a–7f at $\bar{S} = 0.01$ is presented in the fourth row of Table 3. Its value is much smaller than the depth determined from the measurements of the loop diameter in the plane of the sky based on filter images, being typically 1000–2000 km. However, as was noted by Schmieder et al. (1995), the depth of 2000 km may have been overestimated and the real thickness can be somewhat smaller due to the superposition of several loops along the line of sight.

5.3. Determining the Electron Density

The electron density in a loop can be derived from the Hα profiles, because, as Heinzel et al. (1994) and Schmieder et al. (1995) showed, there exists a unique relation between emission measure EM and integrated intensity E(Hα). Then, given the integrated intensity, the electron density can be derived from the expression

$$EM = n_e^2 \times D, \qquad (8)$$

where D denotes the geometrical depth along the line of sight including the filling factor.

The integrated intensity E(Hα) is expressed as

$$E = I_{\mathrm{c}} \int \frac{I_\lambda}{I'_{\mathrm{c}}} d\lambda = I_{\mathrm{c}} W' \,(\text{Å}). \qquad (9)$$

Here, I_{c} is the continuum intensity close to Hα at the solar disk center, $I_{\mathrm{c}} = 2.836\times10^6$ erg cm^{-2} s^{-1} sr^{-1} (in cgs units), and W' (Å) is the integrated intensity of the line normalized to the observed continuum intensity at the solar disk center (I'_{c}).

The line equivalent width W' (Å) obtained from our observations was normalized to I'_{op}, the continuum adjacent to the loop. To obtain W' (Å) in continuum units at the solar disk center, we passed from I'_{op} to $I(\theta)$ and then from $I(\theta)$ to I'_{c}; $I(\theta)$ is the observed continuum intensity at the disk edge. Figure 8 presents I'_{op} and $I(\theta)$ inferred from the intensity measurements across the spectrogram.

Having averaged the measured intensities $I(\theta)$ at a distance from the disk center $\cos\theta = 0.027$, 0.021, and 0.018, we obtained $I'_{\mathrm{op}}/I(\theta) = 0.38$ (Fig. 8). In addition, it is well known (Allen 1973) that $I(\theta)/I'_{\mathrm{c}} = 0.28$ (at $\cos\theta = 0.02$). We then obtain $E = 0.32\times10^6 W'$ cgs, where W' (Å) is the equivalent width derived from our observations. Taking the mean values of W' (Å) for each of the groups in Table 1, we obtained the integrated intensity E (Table 3). To determine the emission measure EM, we used Fig. 8

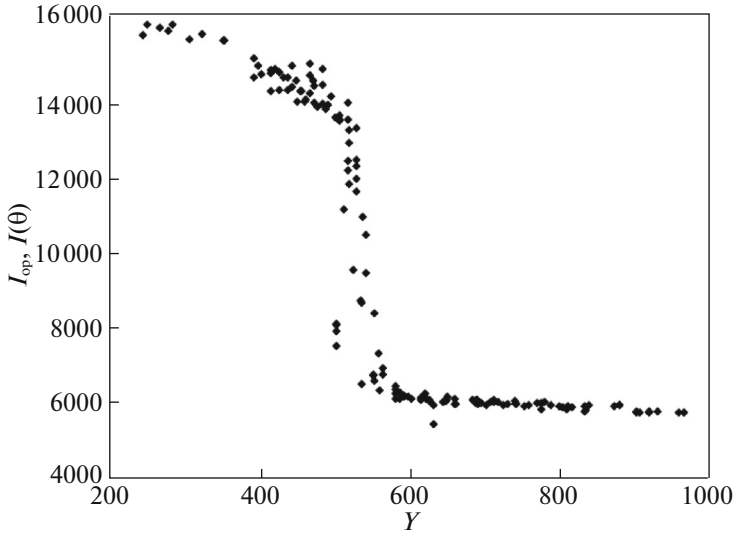

Fig. 8. Dependence of I'_{op} and $I(\theta)$ on distance (in pixel) across the spectrogram.

from Heinzel et al. (1994), where the correlation between $\log E$ and EM calculated for a realistic range of temperatures in Hα loops (8000–15 000 K) for $\xi = 10$ km s^{-1} and two heights, $H = 50\,000$ and 100 000 km, is presented. This allowed us to present the mean emission measures for the three groups of profiles in the table. In addition, the table gives the ratio of the integrated intensity (%) to the solar intensity in Hα at the disk center. For comparison, this ratio in Schmieder et al. (1995) is 3–8%, from which may conclude that the loops we observed were fairly bright. The emission measure (10^{29} cm^{-5}) in Schmieder et al. (1995) was also found to be lower.

We derived the geometrical size of the loop along the line of sight in Eq. (8) from Eqs. (6) and (7). Since the geometrical depth was determined from the optical depth, the size z suggests that this path is completely filled with emitting matter. Actually, this is not the case and the filling factor must be <1; we took two values, 0.5 and 0.3. Using these values, we obtained two values of D and, accordingly, two values of n_e for each group of profiles. The uncertainty in choosing the filling factor is seen to affect insignificantly the determination of the electron density. Moreover, an apparent loop diameter of ~2000 km is occasionally taken as the geometrical depth along the line of sight; in this case, for the three groups the electron density would be $(2.5–7.5) \times 10^{10}$ cm^{-3}. Nevertheless, an electron density close for all three groups and equal, on average, to 10^{11} cm^{-3} seems realistic. Close values of n_e in all groups stem from the fact that an increase (or decrease) in the integrated intensity of the line profiles is accompanied by an increase (or decrease) in the geometrical size of the loop falling on the line of sight.

6. DISCUSSION OF RESULTS AND CONCLUSIONS

Determining the place of the Hα loops in the development of the general scenario for the loops of this Masuda-type flare (Masuda et al. 1994) obtained from RHESSI and SDO/AIA data (Liu et al. 2013) is of interest. Figure 9 presents an image of the loops taken in the time interval between the loop images in the 94 Å line. The spatial resolution of the birefringent-filter image in Hα at the LSVT and the SDO/AIA image near the 94 Å line allows us to see that the loop images in these lines remain similar with a time interval of ~1 h (06:55:56 and 08:02:03 UT). The loops in the arcade are turned so that despite the height difference in the northern part of all three (at 05:25:27 UT too, but with a lower resolution) images, several far arcade loops are clearly visible. It can be seen from the figure that the system of loops in the 94 Å line ascended by ~44″ over the period from 05:25:27 to 08:02:03 UT. This makes it possible to estimate the ascending velocity of the entire loop arcade, ~3.5 km s^{-1}. At the instant the Hα image was taken, the loop in 94 Å was then at a height of 66.″4, i.e., at $\sim 1.9 \times 10^4$ km above the loop top in Hα.

According to Liu et al. (2013), in this flare a vertical current sheet formed between two X-ray sources, and magnetic reconnection ensued within this current sheet, leading to the eruptive M7.7 flare. The distance between the two sources, on average, increased, and the entire configuration ascended with time. Thus, the magnetic reconnection site also ascended. Svestka (1987) also found that the reconnection site ascended with a velocity of 7–8 km s^{-1}.

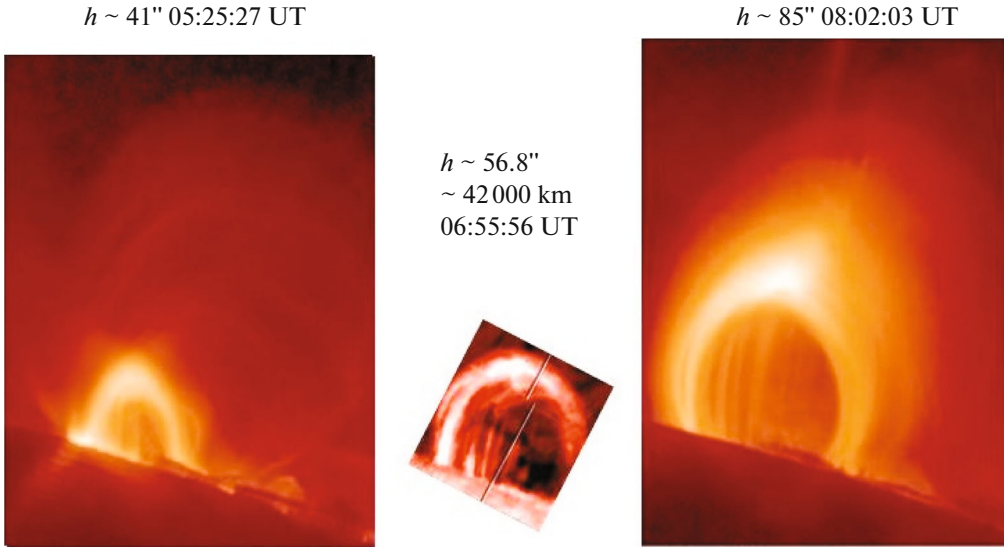

Fig. 9. (Color online) Comparison of the loop images in the 94 Å and Hα lines on the LSVT spectrograph slit.

In this flare magnetic reconnection produced bidirectional outflows in the form of the erupting observed plasmoids and contracting loops. In view of the ascent of the reconnection site, the newly formed loops were produced increasingly high and then contracted. Since the height of the X-ray sources increased, the positions of the newly formed Hα loops must ascend with time. Note that in this flare we found the ascending velocity of the loop arcade to be 3.5 km s^{-1}.

The July 19, 2012 flare is peculiar, because the second X-ray source was clearly seen in it. Therefore, unexpected manifestations in the post-flare loops might also be expected in the optical band. The only thing that may be deemed peculiar is a fairly high electron density, 10^{11} cm^{-3}, several hours after the flare onset. Krucker and Battaglia (2014) obtained such a density for the thermal part of the loop (8×10^{10} cm^{-3}), corresponding to the greatest density in M and X flare loops (Caspi 2014). The integrated intensity, reaching 12%, also turned out to be slightly higher than the mean one (3–8%). On the whole, these data differ insignificantly from the universally accepted ones. However, the results of studying the velocities in these loops (which we are going to do in future) can be of interest.

ACKNOWLEDGMENTS

This work was performed within the Basic Research Program II.16.1 of the Russian Academy of Sciences "Fundamental Problems of Space Weather Processes, Including Processes on the Sun, the Interplanetary Medium, the Earth's Magnetosphere and Atmosphere. The Control and Ecology of Near-Earth Space," project II.16.1.6 "Geoeffective Processes in the Solar Chromosphere and Corona." The experimental data were obtained using the unique scientific facility "Large Solar Vacuum Telescope," registration no. 01-29.

REFERENCES

1. C. W. Allen, *Astrophysical Quantities* (Athlone Press, London, 1973; Mir, Moscow, 1977, p. 446).
2. A. Caspi, S. Krucker, and R. P. Lin, Astrophys. J. **781**, 43 (2014).
3. Q. Chen and V. Petrosian, Astrophys. J. **748**, 33 (2012).
4. N. M. Firstova, V. I. Polyakov, and A. V. Firstova, Solar Phys. **249**, 53 (2008).
5. N. M. Firstova, V. I. Polyakov, and A. V. Firstova, Astron Lett. **40**, 449 (2014).
6. P. A. Gritsyk and B. V. Somov, Astron. Lett. **42**, 531 (2016).
7. P. Heinzel, in *Proceedings of the 3rd SOHO Workshop (ESA SP-373)*, p. 133 (1994).
8. P. Heinzel and M. Karlicky, Solar Phys. **110**, 343 (1987).
9. P. Heinzel, B. Schmieder, and P. Mein, Solar Phys. **139**, 81 (1992).
10. P. Heinzel, P. Gouttenbrose, and J. C. Vial, Astron. Astrophys. **292**, 656 (1994).
11. S. Ishikawa, S. Krucker, T. Takahashi, and R. P. Lin, Astrophys. J. **737**, 48 (2011).
12. S. Kamio, H. Kurokawa, and T. T. Jshii, Solar Phys. **215**, 127 (2003).
13. P. Kotrc, P. Heinzel, A. V. Gorshkov, E. V. Kononovich, Yu. A. Kupryakov, and O. B. Smirnova, in *Proceedings of the IAU Colloq. No. 144 on Solar Coronal Structures,* p. 361 (1994).

14. P. Kotrc, M. Barta, P. Schwarz, Y. A. Kupryakov, L. K. Kashapova, and M. Karlicky, Solar Phys. **284**, 447 (2013).
15. S. Krucker and M. Battaglia, Astrophys. J. **780**, 107 (2014).
16. H. Li, J. You, Q. Du, and X. Yu, Solar Phys. **225**, 75 (2005).
17. W. Liu, Q. Chen, and V. Petrosian, Astrophys. J. **767**, 168 (2013).
18. S. Masuda, T. Kosugi, H. Hara, S. Tsuneta, and Y. Ogawara, Nature **371**, 495 (1994).
19. P. Mein and N. Mein, Astron. Astrophys. **203**, 162 (1988).
20. J. Milic, S. Dejanic, and P. Kotrc, Publ. Astron. Observ. Belgrade **86**, 283 (2009).
21. V. Petrosian, T. Q. Donagny, and J. M. McTiernan, Astrophys. J. **569,** 459 (2002).
22. F. Reale, Living Rev. Solar Phys. **11**, 4 (2014).
23. B. Schmieder, P. Heinzel, J. E. Wilk, J. Lemen, B. Anwar, P. Kotrch, and E. Hiei, Solar Phys. **156**, 337 (1995).
24. V. I. Skomorovsky and N. M. Firstova, Solar Phys. **163**, 209 (1996).
25. H. J. Smith and E. Smith, *Solar Flares* (Macmillan, New York, 1963), p. 424.
26. Z. Svestka, Solar Phys. **121**, 399 (1989).
27. Z. Svestka, J. M. Fontenla, M. E. Machado, S. F. Martin, D. F. Neadig, and G. Poletto, Solar Phys. **108**, 237 (1987).
28. M. Tomchak, Astron. Astrophys. **366**, 294 (2001).
29. M. Tomchak, Astron. Astrophys. **502**, 665 (2009).
30. J. You, E. Hiei, and H. Li, Solar Phys. **217**, 235 (2003).

Translated by V. Astakhov